



**HAL**  
open science

## Scanning small-angle X-ray scattering analysis of the size and organization of the mineral nanoparticles in fluorotic bone using a stack of cards model

Aurélien Gourrier, Chenghao Li, Stefan Siegel, Oskar Paris, Paul Roschger, Klaus Klaushofer, Peter Fratzl

### ► To cite this version:

Aurélien Gourrier, Chenghao Li, Stefan Siegel, Oskar Paris, Paul Roschger, et al.. Scanning small-angle X-ray scattering analysis of the size and organization of the mineral nanoparticles in fluorotic bone using a stack of cards model. *Journal of Applied Crystallography*, 2010, 43 (6), pp.1385 - 1392. 10.1107/S0021889810035090 . hal-01391591

**HAL Id: hal-01391591**

**<https://hal.science/hal-01391591>**

Submitted on 20 Dec 2022

**HAL** is a multi-disciplinary open access archive for the deposit and dissemination of scientific research documents, whether they are published or not. The documents may come from teaching and research institutions in France or abroad, or from public or private research centers.

L'archive ouverte pluridisciplinaire **HAL**, est destinée au dépôt et à la diffusion de documents scientifiques de niveau recherche, publiés ou non, émanant des établissements d'enseignement et de recherche français ou étrangers, des laboratoires publics ou privés.



Distributed under a Creative Commons Attribution - NonCommercial - NoDerivatives 4.0 International License


*This is a preprint version of the accepted manuscript*

Online version: <https://onlinelibrary.wiley.com/doi/full/10.1107/S0021889810035090>

doi: <http://dx.doi.org/10.1107/S0021889810035090>

**Please cite as:** Gourrier, A., Li, L., Siegel, S., Paris, O., Roschger, P., Klaushofer, K., Fratzl, P. (2010). *Scanning small-angle X-ray scattering analysis of the size and organization of the mineral nanoparticles in fluorotic bone using a stack of cards model*, J. Appl. Crystallogr. 43, 1385-92. doi: 10.1107/S0021889810035090

© 2022 This manuscript version is made available under the CC-BY-NC-ND 4.0 license

<https://creativecommons.org/licenses/by-nc-nd/4.0/> 

# Scanning-SAXS analysis of the size and organization of the mineral nanoparticles in fluorotic bone using a stack of cards model

Aurélien Gourrier<sup>abc\*</sup>, Chenghao Li<sup>a</sup>, Stehphan Siegel<sup>a</sup>, Oskar Paris<sup>ad</sup>,  
Paul Roschger<sup>c</sup>, Klaus Klaushofer<sup>c</sup> and Peter Fratzl<sup>a</sup>

<sup>a</sup> Max-Planck Institute of Colloids and Interfaces, Department of Biomaterials, D-14424 Potsdam, Germany

<sup>b</sup> Current address: Laboratoire de Physique des Solides, UMR CNRS 8502 Université Paris Sud, F-91405 Orsay, France

<sup>c</sup> European Synchrotron Radiation Facility, BP 220, F-38043 Grenoble, France

<sup>d</sup> Current address: Institute of Physics, University of Leoben, A-8700 Leoben, Austria

<sup>e</sup> Ludwig Boltzmann Institute of Osteology at the Hanusch Hospital of WGKK and AUVA Trauma Centre Meidling, A-1140 Vienna, Austria

\* Corresponding author: aurelien.gourrier@cnrs.fr

**Synopsis:** A novel procedure is presented for the SAXS analysis of the organization and size of mineral nanoparticles in pathological bone using a stack of cards model.

**Abstract:** A model describing the size and arrangement of mineral particles in bone tissues is used to analyze the results of a scanning SAXS experiment on a pathological bone biopsy. The overall description assumes that the nanometer-sized mineral platelets are arranged in a parallel fashion with possible fluctuations in their relative position, orientation and thickness. This method is tested on a thin sample section obtained from the biopsy of an osteoporotic patient treated with a high cumulative dose of NaF. The mineralization pattern of fluorotic bone is known to exhibit significant differences as compared to healthy bone in terms of density, particle size and organization. This is the first attempt to provide quantitative indicators of the degree of regularity in the packing of the mineral platelets in human pathological bone. Using scanning SAXS with a synchrotron microbeam of 15  $\mu\text{m}$ , we show that our method allows discriminating between pathological and healthy bone at the tissue level. Additionally, we discuss the benefit of this method in the accuracy of particle size determination using SAXS.

**Keywords:** Bone; Nanoscale; Ultrastructure; Mineral particles; Synchrotron radiation; Microbeam; Small-angle scattering; SAXS; Scanning X-ray scattering imaging; Modelling

# 1. Introduction

The structure of bone tissues at the nano-scale is currently receiving considerable attention. This partly results from recent findings showing that the clinical indicators measured at higher hierarchical levels and currently used to characterize various pathologies are, in some cases, insufficient to establish a reliable diagnosis. More specifically, there is growing evidence supporting the view that the micro-architecture and bone mineral density (BMD) alone are not sufficient to determine the risk of fracture in elderly people (Watts, 2002). Therefore, bone material quality is increasingly recognized as a major determinant of bone fragility (Felsenberg & Boonen, 2005; Seeman & Delmas, 2006). A better understanding of the fundamental structure of the tissue is thus required in order to improve medical treatments and therapies.

At this level, the structure of bone is quite heterogeneous due to complex physiological remodelling activities occurring throughout the lifetime of the tissue. Mineralized collagen microfibrils of  $\sim 100$  nm in diameter act as building blocks, packing into complex arrangements of larger scale structures in the form of bone packets or osteons with characteristic dimensions of  $100 \mu\text{m}$  in diameter (see, e.g., Currey, 2002; Fratzl & Weinkamer, 2007). There is a general consensus over the fact that the mineral phase within and around the fibrils is found in the form of thin calcium phosphate platelets of nanometer dimensions (Weiner & Traub, 1986, 1989; Landis & Hodgens, 1996; Fratzl *et al.*, 2004). The size of these nanoparticles in the longitudinal and transverse directions is generally estimated to  $\sim 50$  nm and  $\sim 25$  nm respectively in mature human bone (Robinson, 1952; Weiner & Traub, 1992). The causes for the dispersion in the measured values most likely reside in the constrained mineralization inside the collagen matrix (Hodge & Petruska, 1963; Glimcher & Krane, 1968) as well as in the difficulty in sample preparation and analytical interpretation (Ziv & Weiner, 1994). However, most studies also indicate that the distribution in thickness is relatively narrow, usually falling in the range 2 – 6 nm (Weiner *et al.*, 1991; Rubin *et al.*, 2003). Remarkably, this characteristic length scale has also been found in a wide range of species and organs such as tooth dentin or rein-deer antler (Currey, 2002). Furthermore, the size, structure and distribution of mineral particles has been shown to play a major role in the mechanical behaviour of the bone material (Fratzl *et al.* 2004; Roschger *et al.* 2008). As a result, the thickness of the mineral platelets, their relative orientation and organization across the tissue are important parameters of interest for fundamental and medical studies of bone.

Small-angle X-ray scattering (SAXS) has been used for a long time to characterize size and habit of bone mineral crystals (Fratzl *et al.*, 1991, 1992, 1994, 1996, 1997, 2004). In most of this work, parameters were determined based on invariants of the scattering which do not depend on specific assumptions about the mineral particles, such as their general shape or distribution. The advantage of this approach is that it is fairly generic, while the main drawback is that it only provides a very rough description of the mineral crystals. In particular, the size of the mineral particles has been characterised by the T-parameter which describes the smallest dimension of a particle regardless of its shape. Recently, more refined models were proposed where one includes additional information to describe the SAXS data (Fratzl *et al.*, 2005; Burger *et al.*, 2008; Bunger *et al.*, 2010). Based on electron microscopic evidence (Weiner & Traub, 1992; Landis *et al.*, 1993), these models assume plate-shaped mineral crystals with a regular local parallel arrangement within the collagen microfibrils while a lesser degree of correlation can be expected between the fibrils. The models differ by their assumptions about the size distribution of mineral plates and their spacing but they have the advantage of giving some indication on the distance distribution between particles, in addition to their thickness T.

Recent development of synchrotron x-ray sources with X-ray beams of micrometer size now allows performing scanning-SAXS (sSAXS) experiments to characterize the nano-structure with a scanning resolution comparable to the size of typical heterogeneities in the tissue (Fratzl *et al.*, 1997; Riekel, 2000; Gourrier *et al.*, 2007; Paris, 2008). This is a clear advantage over TEM or AFM for medically oriented studies, for which the measure of an average particle size, spacing and relative orientation over large sample areas is usually preferable to a precise characterization of the particle organization of a very localized part of the tissue.

The application of such techniques is proving extremely useful, for example in studying the effect of osteoporosis treatments on bone material quality (Li *et al.*, 2010), or analysing the structure forming around metallic implants (Bünger *et al.*, 2006).

This study reports the use of one of the stack of cards models (Fratzl *et al.*, 2005) for the semi-automatic analysis of sSAXS from pathological bone treated with NaF. Previous reports (Fratzl *et al.*, 1996, 1997) on such samples qualitatively indicate that important structural modifications occur in the bone deposited during the treatment in the remodeling process. Here we present results that allow to discriminate between healthy and abnormal tissue and quantitatively characterize the changes in the packing of the mineral particles.

## 2. Materials and methods

The sample used in this study was prepared from a transiliac bone biopsy of an 82 yrs old woman with postmenopausal osteoporosis treated for 4 years with NaF (25mg/d). The specimen was fixed and dehydrated in a graded series of ethanol and embedded in methyl methacrylate. The surface of the sectioned bone area was polished using a grinding / polishing device (PM5 Logitech, Glasgow, Scotland) for investigations by quantitative backscattered electron imaging (qBEI), from which the bone mineralization density distribution (BMDD) was determined (Roschger *et al.* 1995; Roschger *et al.*, 1998). Subsequently, a thin section of 20  $\mu\text{m}$  in thickness, containing the same surface, was prepared for sSAXS measurements using a slow-speed diamond saw (Buehler Isomet, Lake Bluff, USA) and sand paper for grinding.

The scattering experiments were conducted at the microfocus beamline ( $\mu\text{Spot}$ ) at BESSY II, Berlin, Germany (Paris *et al.*, 2007). The X-ray beam was monochromatized to a wavelength  $\lambda = 0.984 \text{ \AA}$  ( $E = 12.6 \text{ keV}$ ) with a W/Si multilayer monochromator. Focussing was achieved by means of a toroidal mirror combined with a beam-defining pinhole to a diameter of 15  $\mu\text{m}$  in diameter at sample position. The parasitic scattering was reduced with a guard pinhole of 20  $\mu\text{m}$  in diameter placed close to the sample. The specimens were mounted on a high precision translation stage and visualized through an on-axis microscope. Optical calibration of the beam position was achieved with an accuracy of 2  $\mu\text{m}$  by placing on the sample stage a high-resolution CdWO<sub>4</sub> crystal fluorescing in the visible range. The microscope could be remotely interchanged with a 16-bit charge couple device (CCD) area detector (MarMosaic 225, Rayonix, Evanston, USA) with a 225 x 225 mm<sup>2</sup> square converter screen. The images were recorded with a readout time of 5 s at full resolution, i.e. 3048 x 3048 pixels with a pixel size of 73.24 x 73.24  $\mu\text{m}^2$ . The sample-to-detector distance, the detector tilt and the beam centre were calibrated using a silver behenate standard (Blanton *et al.*, 1995).

The 2D data were azimuthally and radially integrated using the FIT2D software package (Hammersly, 1997). The 1D profiles were corrected for the dark current of the CCD and for the parasitic scattering. This procedure and the subsequent analysis were carried out using a dedicated SAXS analysis library written in Python by one of the authors (A. Gourrier). This code essentially relies on the SciPy (Jones *et al.*, 2001) and Matplotlib (Barret *et al.*, 2005) libraries for the analysis and imaging parts. The relative degree of orientation (so-called  $\rho$  parameter) as well as the average direction of the mineral particles were calculated using the azimuthal profiles as described in previous studies (Fratzl *et al.*, 1996). This procedure involves fitting the azimuthal profile using Gaussian functions and a linear base line to account respectively for the fractions of oriented and unoriented particles. The relative degree of orientation is then expressed as the ratio of the areas of the peak to the intensity below the base line. Finally, the average orientation is calculated as the average value of the Gaussian peak positions taking into the account the symmetry of the SAXS signal. The analysis of the radial profiles is more complex and will therefore be described in detail in the following section. The programme MPFIT was used to fit our data. This procedure involves a least-square minimization of the statistically weighted total  $\chi^2$  value based on a Levenberg-Marquardt algorithm (Markwardt, 2008). The goodness of the fit was assessed by calculating the coefficient of determination ( $R^2$ ).

### 3. Theoretical description of the organization of the nanoparticles in bone

In dealing with the SAXS analysis of bone, we recall the basic assumption usually made on the tissue consisting of a two-phased media with nanometer size mineral inclusions embedded in a collagen matrix. This organization is described schematically in Fig.1. The particles are oriented in preferred directions, which lead to an elliptical SAXS pattern on a 2D detector (Fratzl *et al.*, 1991, 1992). Experimentally, the signal acquisition is limited at small angles by the size and position of the beamstop and at large angles by the outer diameter and location of the CCD camera. Typically, the resolution in reciprocal space is in the order of  $q = q_{min} - q_{max} = 0.2 - 3 \text{ nm}^{-1}$  corresponding roughly to  $d = 1 - 30 \text{ nm}$  in direct space. The length of the scattering vector  $q$  is defined as  $q=4\pi\sin\theta/\lambda$  where  $2\theta$  is the scattering angle.

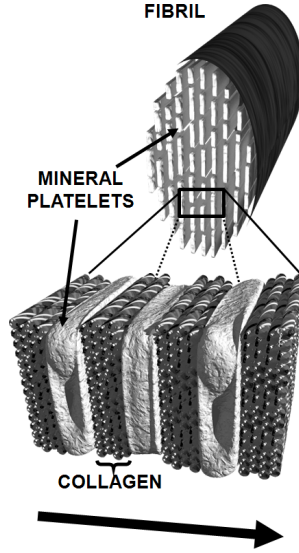


**Figure 1.** Schematic illustration of the fibril structure showing the internal arrangement of mineral platelets separated by layers of collagen molecules in a 'stack of cards' fashion. The short-range order results in a strong positional correlation of the mineral platelets along the direction normal to the faces indicated by the arrow. The fluctuations in position and thickness of the platelets and organic layers along this axis can adequately be described by a one-dimensional Poisson distribution. In the other two directions, there is no experimental evidence for such short-range order.

#### 3.1. Estimation of the particle width using integral parameters

The average thickness of the particles in the volume probed by the beam can be expressed as the ratio of the volume fraction of mineral  $\phi$  to the total surface per unit volume of tissue  $\sigma$ :

$$T = \frac{4\phi(1-\phi)}{\sigma} \quad (1)$$

Assuming a two-phased system with sharp interfaces and a mineral volume fraction  $\phi$  of 50 %, this quantity can be calculated from the radial SAXS profile using the following expression (Fratzl *et al.*, 1991, 1992, 1996):

$$T = \frac{4J}{\pi P} \quad (2), \text{ where } P = \lim_{q \rightarrow \infty} (q^4 I(q)) \quad (3) \text{ and } J = \int_0^{\infty} q^2 I(q) dq \quad (4)$$

This so-called  $T$ -parameter was first introduced by Porod (Porod, 1951, 1952) and has the advantage of being independent of the shape and arrangement of the particles.

The first limitation in this procedure comes from the determination of the Porod constant  $P$  which can only be calculated using a restricted part of the scattering curve at high  $q$  values known as the Porod region. Furthermore, the scattered intensity  $I(q)$  also contains a constant contribution from the incoherent and inelastic scattering.

Hence, Porod's law can be expressed as  $I(q) = P/q^4 + L$ , where  $L$  is a constant. Therefore,  $P$  and  $L$  are respectively determined by linear regression of the curve  $I(q)q^4$  vs  $q^4$  at high  $q$  values. Although the choice of the lower limit of the Porod region is known to be critical for the determination of  $P$ , this limiting step can be partly overcome by fitting the  $\log(I(q))$  vs  $\log(q)$  curve in the corresponding region where a slope of  $-4$  is expected.

An additional limitation lies in the experimental restrictions of the accessible  $q$ -range. This implies that the only part of the integral parameter  $J$ , defined in equation (4), which can be measured in this range is:

$J_{\text{exp}} = \int_{q_{\text{min}}}^{q_{\text{max}}} q^2 I(q) dq$ . At high  $q$ , the experimental curve can be extrapolated using Porod's law (equation (3)). In

this case,  $J_{\text{Porod}} = \int_{q_{\text{max}}}^{\infty} q^2 I(q) dq = P/q_{\text{max}}$ . However, there is no rigorous way to account for the missing data at low  $q$ . Two approximations are generally used assuming either a linear decrease or a constant extrapolation of

the intensity at  $q = 0$ , where  $J_{\text{min}} = \int_0^{q_{\text{min}}} q^2 I(q) dq$  gives respectively  $J_{\text{min1}} = q_{\text{min}}^3 I(q_{\text{min}})/2$ , or

$J_{\text{min2}} = q_{\text{min}}^3 I(q_{\text{min}}) = 2J_{\text{min1}}$ . From this, it follows that:  $J = J_{\text{min}} + J_{\text{exp}} + J_{\text{Porod}}$ .

In order to overcome these limitations, an alternative approach has been developed, making use of models which will be described in the following sections.

### 3.2. Analysis of the mineral arrangement using a stack of cards model

Assuming that the T-parameter has been calculated, all the information about the shape and arrangement of the nanoparticles is contained in a rescaled function of the dimensionless parameter  $x = qT$  (Fratzl *et al.*, 1996), defined as:

$$G(x) = x^2 I(x/T) / (JT^3) \quad (5), \text{ where } \int_0^{\infty} G(x) dx = 1 \quad (6).$$

Systematic changes in  $G(x)$  curves have been found with differing species, bone age or volume fraction of mineral (Fratzl *et al.*, 1996). Such differences seem to be very consistent throughout the existing literature and indicate some systematic differences between tissue structures. These observations entailed the need for the development of structural models to describe the  $G(x)$  curves and thus the organization of the mineral phase.

Since the particles are mostly found in the form of parallel platelets, a model describing the arrangement of particles as stacks of cards has been developed to fit the  $G(x)$  curve and thus provide sets of parameters describing the organization at this structural level (Fratzl *et al.*, 2005) and later modified with different assumptions by Burger *et al.* (2008). Here we use the first of the two models which has fewer parameters and simpler analytic expressions, but, yet, still provides good fits of the data and provides quantitative indicators for the nanoparticle ordering. This model assumes that the mineral particles are positioned along the direction normal to the platelets (indicated by an arrow in Fig. 1). The function  $G(x)$  is related to the normalized (one-dimensional) correlation function  $g(\zeta)$  by a Fourier transform (Fratzl *et al.*, 2005)

$$G(x) = \frac{2}{\pi} \int_0^{\infty} g(\zeta) \cos(\zeta x) d\zeta \quad (7)$$

The simplest assumption, which we are considering here, is to describe the correlation function as a damped oscillation:

$$g(\zeta) = A e^{-\alpha\zeta} \cos(\beta\zeta - \varphi) \quad (8)$$

The period of the oscillation  $2\pi/\beta$  describes the typical spacing between particles (in units of  $T$ ) and the exponential decay (parameter  $1/\alpha$ ) describes the distance over which the periodicity in particle spacing is damped. The normalization of  $G(x)$  given by eqs.(5) and (6), which can equivalently be written as (Fratzl et al., 2005)  $g(0)=1$  and  $\partial g/\partial \zeta(0)=-2$ , immediately defines the other two constant as  $A=1/\cos\varphi$  and  $\tan\varphi=(\alpha-2)/\beta$ . This leads to simple model functions for  $G(x)$  and for  $g(\zeta)$  in the form:

$$g(\zeta) = \exp^{-\alpha\zeta} \left[ \cos(\beta\zeta) + \frac{\alpha-2}{\beta} \sin(\beta\zeta) \right] \quad (9)$$

$$G(x) = \frac{4}{\pi} \frac{x^2 + (\alpha-1)(\alpha^2 + \beta^2)}{(x^2 + \alpha^2 - \beta^2)^2 + 4\alpha^2\beta^2} \quad (10)$$

Due to the construction of the model, the parameter  $\beta$  describes the degree of spatial correlation between successive plates, separated by an average distance  $d = T.2\pi/\beta$ . The other parameter,  $\alpha$ , controls the damping of the oscillations and, therefore, provides an indication on the relative extent of the ordering. Smaller values of  $2\pi/\alpha$  point to a reduction in the short-range ordering of the platelets (greater disorder). As a result, at constant  $T$  values,  $\beta/\alpha$  can be seen as a reasonable (scalar) indicator of the degree of ordering since the degree of spatial correlation is then modulated by the relative extent of the short-range order.

Previously, it had been shown that the absence of positional correlation between the plates would result in (Fratzl, 1994):

$$g(\zeta) = \exp^{-2\zeta} \quad (11)$$

and

$$G(x) = \frac{4}{\pi} \frac{1}{x^2 + 4} \quad (12),$$

which corresponds to the special case of equations (9) and (10) where  $\alpha = 2$  and  $\beta = 0$ . In cases where the particles are strongly disorganized, the  $G(x)$  curve can, therefore, be expected to have a Lorentzian shape.

### 3.3. Model based refinement of the particle size and order parameters

From a practical point of view, fitting the stack of cards model to the  $G(x)$  curves obtained from the experimental data  $I(q)$  using equation (10), implies that the parameters  $\alpha$  and  $\beta$  will be biased by the approximation at low  $q$  in the calculation of  $J_{min}$ . In order to avoid this error propagation, it is therefore preferable to fit the unbiased experimental data using equation (5) rewritten as:

$$q^2 I(q) = \frac{\pi}{4} P T^2 G(x) \quad (13)$$

using the expression of  $G(x)$  given in equation (10) with  $x = qT$ .  $P$  is then a fixed parameter, since it is calculated independently from the model, while  $T$  is allowed to vary to account for the unknown value of  $J_{min}$ . It can thus be expected that this procedure will yield a better estimate of  $T$  than under the initial assumptions.

From the previous considerations, it also follows that the parameter  $\beta/\alpha$  defined previously is insufficient to characterize the degree of ordering since it does not take into account the uncertainty in  $J_{min}$ . We propose to use a new parameter,  $\kappa$ , defined as:

$$\kappa = \frac{\beta T_{ref}}{\alpha T} \quad (14)$$

where  $T_{ref}$  is a reference value of  $T$  that can be obtained either from a reference sample (e.g. control), from a region of interest of the scan considered to be representative of the healthy tissue or even from the mean  $T$  value of the scan. A previous study using this model to fit SAXS data from healthy bone lead to values of  $\beta/\alpha \sim 1$  (Fratzl *et al.*, 2005), thus implying that  $\kappa \sim 1$ , since  $T \sim T_{ref}$  in this case. Inversely, a strong disorganization should yield  $\kappa = 0$  since, as seen in section 3.2,  $\beta = 0$  in such a case.

## 4. Results

A quantitative back-scattered electron microscopy image (qBEI) of the sample used for this study is shown in Fig. 2a. The grey levels are proportional to the local mineral content of the bone matrix, brighter pixels indicating a higher mineral density. The trabecular feature displays a central part (roughly running vertically through the sample) which strongly differs from the adjacent bone packets. The compact and homogeneously mineralized bone matrix in the central part has the aspect of normal, healthy bone. The peripheral tissue, on the other hand, exhibits a higher mineral density albeit with a greater amount of mineralization defects. Altogether, the presence, throughout the whole biopsy, of an important fraction of more highly mineralized bone packets results in a significant shift in the bone mineralization density distribution (BMDD) curve towards higher mineral content as shown in Fig. 2d (Roschger *et al.*, 2008).

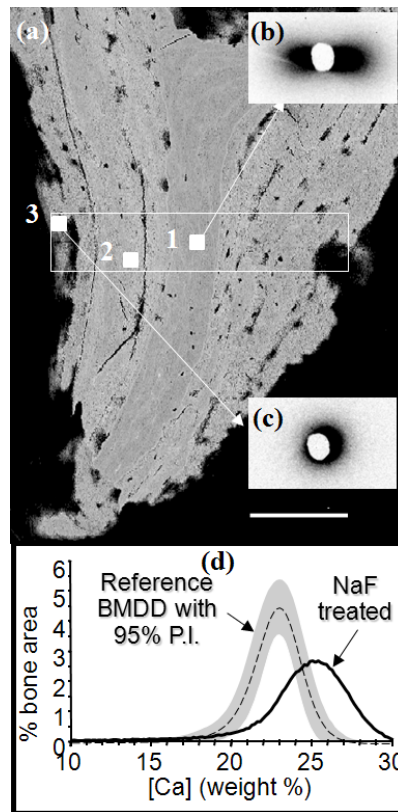


**Figure 2.** (a) qBEI image of a region of interest of a sample section prepared from a transiliac bone biopsy of an 82 years old osteoporotic woman treated with NaF. The rectangle indicates the area scanned with an X-ray beam of  $15\mu\text{m}$  in diameter. The size of the region probed by the microbeam is indicated by the square dots enlarged by a factor of 2 for clarity. The scale bar indicated at the bottom is  $200\mu\text{m}$ . Examples of the 2D SAXS pattern obtained in the centre of the sample and on the left edge are shown respectively in (b) and (c). The BMDD deduced from the grey level histogram of the qBEI image of the whole sectioned compartment of the biopsy is shown as a solid line in (d). A reference curve (Roschger *et al.*, 2008) is also indicated as a dashed line and the grey contour represents a 95% prediction interval (P.I.) for healthy bone.



To analyse the structural differences across the sample, a region of interest of 600 (h) x 105 (v)  $\mu\text{m}^2$  indicated by the rectangle in Fig. 2a was selected using an online microscope and scanned in steps of 15 (h) x 15 (v)  $\mu\text{m}^2$ . Since the size of the scan steps corresponds to the beam diameter at sample position, this indicates a full resolution map of the area. The SAXS patterns obtained in the central and surface parts, shown respectively in Fig. 2b and Fig. 2c are quite different.

The first is typical for strongly oriented bone showing an overall elliptical aspect, while the circular shape of the second tends to indicate a lesser degree of orientation in the volume probed by the beam. This is a good indication for a stronger texture in the centre and a much less organized structure at the edges of the sample. This observation is confirmed by the examination of the corresponding Kratky plots,  $q^2I(q)$  vs.  $q$ , shown in Fig. 3. The data Fig. 3a (corresponding to position 1 in Fig. 2a) exhibits a clear maximum and seems to decrease towards low  $q$ -values while the curve in Fig. 3c (position 3 in Fig. 2a) has a pronounced Lorentzian shape with a maximum at  $q = 0$ . Similar observations were made in previous studies, pointing towards a disorganization of the ultrastructure of the tissue in the second case (Fratzl *et al.*, 1994, 1996; Roschger *et al.*, 1997). The data in Fig. 3b (position 2 in Fig. 2a.) are somewhat intermediate since no clear maximum is found but there is an inflection point indicating a possible decrease below the resolution limit.

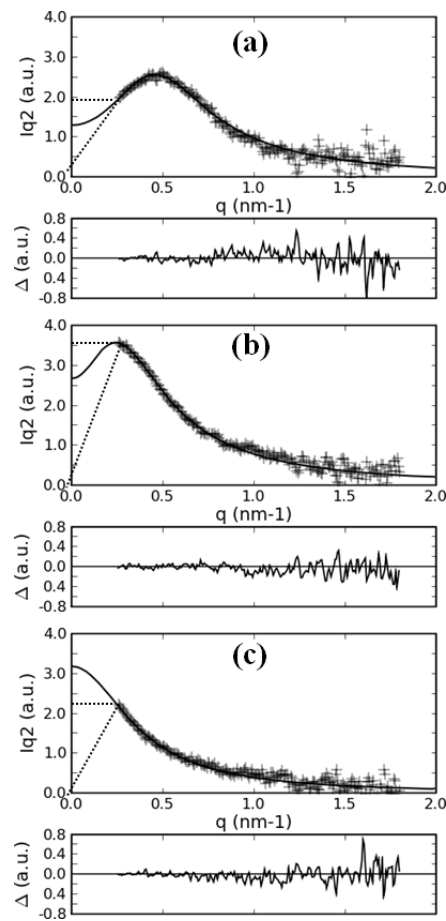


**Figure 3.** Representative set of experimental Kratky data,  $I(q)q^2$  vs.  $q$  (crosses), and result of the fitting procedure (solid curves) using the solution of the 'stack of cards' model described by equations (13) and (10). The difference profile calculated in the data range is shown below each plot. Additionally, the usual approximations made at low  $q$  in the calculation of  $J_{\text{min}}$  are indicated by dotted lines. The data in (a), (b) and (c) were respectively acquired at positions 1, 2 and 3 in Fig. 2a.

In order to derive quantitative information on the particle arrangement, the Kratky curves  $q^2I(q)$  vs.  $q$  were fitted using equation (13) within a range of  $q = 0.2\text{--}3 \text{ nm}^{-1}$ . In order to test the robustness of the fits, this procedure was repeated with a large range of initial parameters  $\alpha_i$  and  $\beta_i$ . This showed that equation (13) was sufficient to provide a good fit for all the data, despite substantial differences in the shapes of the Kratky curves. This is illustrated in Fig. 3a, 3b, 3c where the fitted parameters were respectively  $\alpha = 1.44$ ,  $\beta = 1.63$  ( $R^2 = 0.962$ ),  $\alpha = 1.37$ ,  $\beta = 0.77$  ( $R^2 = 0.985$ ) and  $\alpha = 2.00$ ,  $\beta = 0$  ( $R^2 = 0.940$ ). It is worth noting that the later case corresponds to the conditions leading to equation (12) indicating a total loss of positional correlation of the platelets.

A summary of the results is shown in Fig. 4 in the form of a plot of  $2\pi/\alpha$  vs.  $d = T \cdot 2\pi/\beta$ . This implies that the fits leading to a solution where  $\beta = 0$  were discarded in these graphs. The first striking observation is that the data obtained in the central part of the sample (open circles) can clearly be distinguished from those obtained in the rest of the scan (closed circles). Interestingly, the first group of data are centred within a narrow range about a value of  $d \sim 17 \pm 2 \text{ nm}$  while the second are much more scattered towards higher values of  $d = 25\text{--}50 \text{ nm}$ . This tends to show that there is a very sharp distribution of inter-particle distances in the central part while a progressive loss of correlation is observed elsewhere in the sample. Note that, as previously stated, these two groups yield different mineral volume fractions. Secondly, most of the data fall in a range of  $2\pi/\alpha = 3.5 \pm 1.5$  which implies that, even for the central part of the sample where the platelets have a high degree of spatial coherence, there are some fluctuations in the extent of the short-range order.

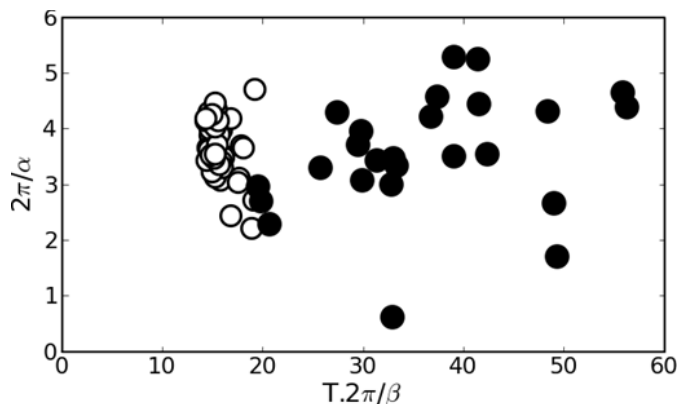


**Figure 4.** Plot of  $2\pi/\alpha$  vs.  $d = T \cdot 2\pi/\beta$ . The open and closed circles represent respectively the results of the fit of the data collected in the central part of the sample and in the rest of the scanned area.

To put these results in perspective, a map of the  $T$ -parameter calculated from the model is shown in Fig. 5a. The values in the central part of the sample are close to  $T \sim 4 \text{ nm}$ , a typical value for healthy bone (Fratzl *et al.*, 2004; Roschger *et al.*, 2008). In the rest of the sample, 'patches' can be observed where  $T \sim 4.5\text{--}5.5 \text{ nm}$  indicating larger crystal sizes. These patches are separated by regions where  $T \gg 10 \text{ nm}$  appearing in bright on the map due to scaling. Such values are quite unusual and most likely result from an abnormal mineralization process. Based on these observations, the degree of ordering,  $\kappa$ , was calculated from equation (14) with  $T_{ref} = 4 \text{ nm}$  (Fig. 5b). A clear distinction can be observed between the central region where  $\kappa \sim 0.9\text{--}1.0$  and the rest of the scanned area where  $\kappa \sim 0$  for  $> 90 \%$  of the data, indicating a total disorganization of the mineral platelets. The remaining values fall in a range  $0 < \kappa < 1$ . A complementary analysis of the orientation of the particles was undertaken as described in section 2. This is illustrated by the vector map in Fig. 5c. The particles are arranged in a very parallel fashion with a high degree of alignment in the central part of the tissue while a close to random orientation is found near to the sample surfaces, on the extreme left and right hand side of the image. In volumes closer to the centre, there are still regular patterns in the orientation of the particles, although gradually losing the original vertical direction towards the edges of the sample. It is worth noting that the spatial resolution of the scan, given by the size of the X-ray beam at sample position, is sufficiently high in this study ( $15 \mu\text{m}$ ) to obtain fine maps of the bone packets. The results shown in Fig. 5 can therefore be interpreted at the level of the individual bone packets which are the areas replaced during a single remodelling event.

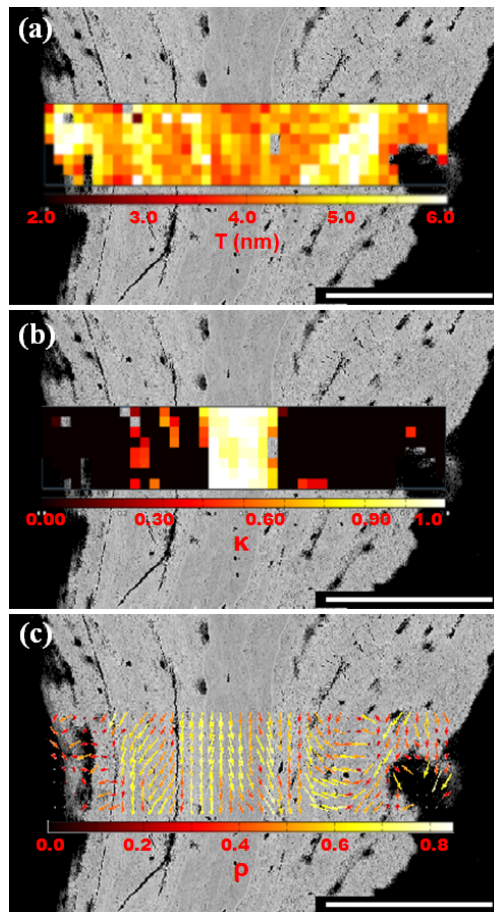


**Figure 5.** A map of the T-parameter in the scanned area is shown in (a) and corresponding parameter  $\kappa$  in (b) with appropriate scaling. Similarly, the average orientation of the mineral particles at each position of the scan is shown in (c) in the form of vectors. The direction of the vectors indicate the average orientation of the mineral particles in the volume probed by the beam while their length and colour correspond to the relative degree of orientation  $\rho$ . The scale bar indicated at the bottom is 200  $\mu\text{m}$ .

## 5. Discussion

We have investigated the biopsy of an osteoporotic patient treated for 4 years with NaF using microbeam small-angle X-ray scattering. The results presented in the previous sections reveal that the ultrastructure of the vertical central part of the sample is close to that of healthy bone, while the rest of the tissue is much more disorganized. It is therefore most likely that the former part was produced prior to the medical treatment, and the latter was formed during the ingestion of NaF by the patient. Interestingly, this implies that the central part was essentially unaffected by the treatment, as could have been postulated, e.g. by diffusion of important quantities of Fluoride ions into the hydroxyapatite particles. This is in agreement with previous work conducted in the field (Grynopas, 1990; Bang & Baud, 1990). Only those parts of the bone which were remodelled during the treatment are affected and show a strongly modified nanocomposite structure with larger mineral crystals (Fratzl *et al.*, 1994).

The model proposed in this study turns out very successful in discriminating between healthy and pathological bone. Fig. 3 shows that the Kratky plot of the data (and hence  $G(x)$ ) is significantly different in fluorotic bone. Nevertheless, the fitting procedure was found to be very stable, even in the case of strongly disorganized bone, leading to a rapidly converging result. Furthermore, the fact that this model provides a relatively simple analytical solution made it possible to process a large quantity of data in batch mode, thus allowing us to produce maps of the degree of ordering,  $\kappa$ , on a scale comparable to histological images.

The use of this model has yet another important advantage in providing a more realistic estimate of the  $T$ -parameter, and thus of the integral value  $J$  below the resolution limit of the instrument, than would be obtained under the usual assumptions described in section 3.1. This is schematically illustrated in Fig. 3 where the dotted lines represent the two approximations generally used in the calculation of  $J_{min}$ : the horizontal line is a constant extrapolation of  $q_{min}^2 I(q_{min})$  at  $q = 0$  ( $J_{min2}$ ) and the diagonal line assumes a linear intensity decrease to  $q = 0$  ( $J_{min1}$ ). In the case of healthy bone,  $J_{min1}$  and  $J_{min2}$  will provide lower and upper bounds of the model value:  $J_{min1} < J_{model} < J_{min2}$  (Fig. 3a). However, if severe disorganization of the tissue occurs, then the two extrapolations will clearly underestimate the model value:  $J_{min1} < J_{min2} \ll J_{model}$  (Fig. 3c). More recently, Bunger *et al.* (2010) proposed a new model to calculate the  $T$ -parameter in which neither  $J$  nor the Porod constant  $P$  need to be derived. This method could provide an advantage in dealing with data with poor statistics at high  $q$  values as, for example, measurements performed with laboratory sources. However, with the generalization of the use of synchrotron radiation, we believe that the estimation of the Porod constant can be performed with sufficient statistical accuracy. A difference map between the  $T$ -parameter calculated with the stack of cards model and with the classical approach is shown in Fig. 6. Overall, the values obtained using the model are always higher. However, the difference in the central part of the sample is very small, with  $\Delta T < 0.5$  nm, i.e.  $< 10\%$ , which means that the classical approach provides reasonable estimates for healthy bone. On the other hand, the values obtained in the rest of the sample are generally higher by  $\Delta T = 0.7$ -1. nm, i.e. 18-25% and up to  $\Delta T > 1.5$  nm, i.e.  $> 38\%$  in the brightest regions. The use of our model therefore seems clearly beneficial when analysing bone with severe structural pathological alteration.

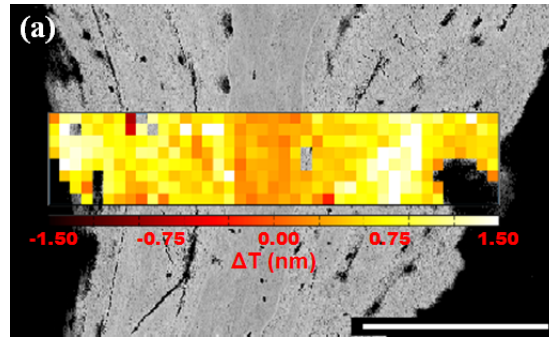


**Figure 6.** Difference map between the  $T$ -parameter calculated with the stack-of-cards model and the values obtained with the integral parameters using equation (2). The scale bar at the bottom is 200  $\mu\text{m}$ .

## 6. Conclusion

The procedure described in this paper represents an improvement in the quantitative description of the organization of bone tissues at the nanometer scale. A more reliable measure of the average mineral particle size was obtained using a model describing the arrangement of the platelets as a regular stack of cards. This model is very close to the description of the tissue's ultrastructure found in the literature and is relatively simple, yielding an analytical solution for the scattering curves. In particular, new parameters were derived to characterize the fluctuations in positional correlation of the particles. Using X-ray microbeams from a second generation synchrotron source, we were thus able to discriminate between healthy and pathological bone with a resolution comparable to histological observations. This allowed to evidence severe structural changes in the bone packets deposited during an anti-osteoporotic treatment based on the administration of NaF.

## References

- Barret, P., Hunter, J. D. & Greenfield, P. (2005). Matplotlib – A Portable Python Plotting Package. In Proceedings from the Astronomical Data Analysis Software & Systems XIV Conference. San Francisco: Astronomical Society of the Pacific.
- Bünger, M. H., Foss, M., Erlacher, K., Li, H., Zou, X., Langdahl, B. L., Bünger, C., Birkedal, H., Besenbacher, F. & Pedersen, J. S. (2006). *Eur. Cell. Mater.* 12, 81–91.
- Bünger, M. H., Oxlund, H., Hansen, T. K., Sørensen S., Bibby, B. M., Thomsen, J. S., Langdahl, B. L. Besenbacher, F., Pedersen, J. S., Birkedal, H. (2010). *Calcif. Tissue Int.* 86, 294–306.
- Burger, C., Zhou, H. W., Wang, H., Sics, I., Hsiao, B. S. Chu, B., Graham, L. & Glimcher, M. J. (2008). *Biophys. J.* 95, 1985–1992.
- Blanton, T. N., Huang, T. C., Toraya, H., Hubbard, C. R., Robie, S. B., Louër, D., Göbel, H. E., Will, G., Gilles, R. & Raftery, T. (1995). *Powder Diffr.* 10, 91–95.
- Bang, S. & Baud, C. A. (1990). *J. Bone Miner. Res.* 5, S87-S89.
- Currey, J. D. (2002). *Bones: Structure and Mechanics*. Princeton, NJ: Princeton University Press.
- Fratzl, P., Fratzl-Zelman, N., Klaushofer, K., Vogl, G. & Koller, K. (1991). *Calcif. Tissue Int.* 48, 407–413.
- Felsenberg, D., Boonen, S. (2005). *Clin. Ther.* 27, 1–11.
- Fratzl, P., Groschner, M., Vogl, G., Plenk, H. Jr, Eschberger, J., Fratzl-Zelman, N., Koller, K. & Klaushofer, K. (1992). *J. Bone Miner. Res.* 7, 329–334.
- Fratzl, P. (1994). *J. Stat. Phys.* 77, 125–143
- Fratzl, P., Roschger, P., Escheberger, J., Abendroth, B. & Klaushofer, K. (1994). *J. Bone Min. Res.* 9, 1541–1549.
- Fratzl, P., Schreiber, S., Roschger, P., Lafage, M. H., Rodan, G. & Klaushofer, K. (1996). *J. Bone Min. Res.* 11, 248–253.
- Fratzl, P., Jakob, H. F., Rinnerthaler, S., Roschger, P. & Klaushofer, K. (1997). *Progr. Colloid Polym. Sci.* 130, 33–39.
- Fratzl, P., Gupta, H. S., Paschalis, E. P., Roschger, P. (2004). *J. Mater. Chem.* 14, 2115–2123.
- Fratzl, P., Gupta, H. S., Paris, O., Valenta, A., Roschger, P., Klaushofer, K. (2005). *Progr. Colloid Polym. Sci.* 130, 33–39.
- Fratzl, P., Weinkamer, R. (2007). *Prog. Mater. Sci.* 52, 1263–1334.
- Glatzer, O. & Kratky, O. (1982). Editors. *Small-Angle X-ray Scattering*. New York: Academic Press.
- Glimcher, M. J. & Krane, S. M. (1968). in *Treatise on Collagen*, edited by B.S. Gould, vol. 2, part B, pp 67–251. New York: Academic Press.
- Gourrier, A., Wagermaier, W., Burghammer, M., Lammie, D., Gupta, H. S., Fratzl, P., Riekel, C., Wess, T. J. & Paris, O. (2007). *J. Appl. Crystallogr.* 40, s78–s82.
- Grynblas, M. D. (1990). *J. Bone Min. Res.* 5, s169–s175.
- Guinier, A. & Fournet, G. (1955). *Small-angle scattering of X-rays*. New York: John Wiley.
- Hammersley, A. P. (1997). ESRF Internal Report No. ESRF97, HA02T. European Synchrotron Radiation Facility, Grenoble, France.
- Hodge, A. & Petruska, J. A. (1963). *Aspects of Protein Structure*, edited by G. N. Ramachandran, pp. 289–300. New York: Academic Press.
- Jones, E., Oliphant, T., Peterson, P. (2001). *SciPy: Open Source Scientific Tools for Python*, <http://www.scipy.org>.
- Landis, W. J., Hodgens, K. J., Arena, J., Song, M. J., McEwen, B. F. (1996). *Microsc. Res. Tech.* 33, 192–202.
- Landis, W. J., Song, M. J., Leith, A., McEwen, L. and McEwen, B. F. (1993). *J. Struct. Biol.* 110, 39–54.
- Li, C., Paris, O., Siegel, S., Roschger, P., Paschalis, E. P., Klaushofer, K., Fratzl, P. (2010). *J. Bone Min. Res.* In press
- Markwardt, C. B. (2008). Non-Linear Least Squares Fitting in IDL with MPFIT. In *Proc. Astronomical Data Analysis Software and Systems XVIII*, edited by D. Bohlender, P. Dowler & D. Durand, vol. 411, pp 251–254. Quebec, Canada, ASP Conference Series.
- Paris, O. (2008). *Biointerphases 3*, FB16–FB26
- Porod, G. (1951). *Kolloid Z.* 124, 83–113.
- Porod, G. (1952). *Kolloid Z.* 125, 51–57.
- Riekel, C. (2000). *Rep. Prog. Phys.* 63, 233–262.

- Robinson, R. A. (1952). *J. Bone Joint Surg.* 34A, 389–434.
- Roschger, P., Plenck, H., Klaushofer, K., Eschberger, J. (1995). *Scanning Microsc.* 9, 75–88.
- Roschger, P., Fratzl, P., Klaushofer, K. & Rodan, G. (1997). *Bone* 20, 393–397.
- Roschger, P., Fratzl, P., Eschberger, J., Klaushofer, K. (1998). *Bone* 23, 319–326.
- Roschger, P., Paschalis, E. P., Fratzl, P., Klaushofer, K. (2008). *Bone* 42, 456–466.
- Rubin, M. A., Jasiuk, L., Taylor, J., Rubin, J., Ganey, T., Apkarian, R. P. (2003). *Bone* 33, 270–282.
- Paris, O., Li, C., Siegel, S., Weseloh, G., Emmerling, F., Riesemeier, H., Erko, A., & Fratzl, P. (2007). *J. Appl. Crystallogr.* 40, s466–s470.
- Seeman, E., Delmas, P. D. (2006). *N. Engl. J. Med.* 354, 2250–2261.
- Traub, W., Arad, T. & Weiner, S. (1989). *Proc. Natl. Acad. Sci. U.S.A.* 86, 9822–9826.
- Traub, W., Arad, T. & Weiner, S. (1992). *Connect. Tissue Res.* 28, 99–111.
- Watts, N. B. (2002). *J. Bone Min. Res.* 17, 1148–1150.
- Weiner, S. & Traub, W. (1986). *FEBS Lett.* 206, 262–266.
- Weiner, S. & Traub, W. (1989). *Connect. Tissue Res.* 21, 259–265.
- Weiner, S., Arad, T., Traub, W. (1991). *FEBS Letters* 285, 49–54.
- Weiner, S. & Traub, W. (1992). *FASEB J.* 6, 879–885.
- Ziv, V. & Weiner, S. (1994). *Connect. Tissue Res.* 30, 165–175.